CrossMark

REGULAR PAPER

Jinxiang Xi · **Tiancheng Yang** · **Khaled Talaat** · **Tianshu Wen** · **Yu Zhang** · **Scott Klozik** ·
Shannon Peters

Visualization of local deposition of nebulized aerosols in a human upper respiratory tract model

Abstract Knowing aerosol deposition distribution (ADD) in the respiratory tract is crucial in assessing dose–response relationship and optimizing inhalation therapy. However, characterization of ADD inside the airway is challenging, due to its inaccessibility to standard measurement instruments. Radioactive imaging techniques such as gamma scintigraphy, SPECT, and PET are capable of characterizing ADD and have proven valuable in drug-device designs, but these techniques are costly, complex-to-use, and pose radiation risks to patients. The objective of this study is to develop and validate a simple and practical technique to visualize nebulized aerosol deposition in a human airway model. An anatomically accurate mouth–lung airway model was used in both experiments and numerical simulations for validation purpose. A sectional hollow cast replica was developed and fabricated using 3D printing. Sar-Gel was utilized to visualize the aerosol deposition distribution on the inner walls of the upper respiratory airway. Computational simulations were conducted to understand the underlying mechanisms of particle transport and deposition. The deposition distribution obtained from the Sar-Gel experiments and numerical simulations resembled each other to a high degree. Specifically, the deposition hot spots in the upper trachea were nearly identical between experiment and simulation, suggesting that the computational model is adequate in capturing the mechanisms of particle transport and deposition. Considering the inhalation effect, more drug particles were delivered to the lungs at 10 L/min than at 30 L/min. The Sar-Gel based method in combination with sectional upper airway casts appears to be a practical approach to visualize regional depositions with nebulizers. Computational modeling and Sar-Gel tests can be used as complementary in optimizing inhalation therapies.

Keywords Pulmonary delivery · Aerosol deposition distribution (ADD) · Mesh nebulizer · Dose–response · Sar-Gel visualization

1 Introduction

The deposition of inhaled particles can be highly heterogeneous in the respiratory tract. A key aspect in inhalation therapy is to determine where the drug particles deposit and how many particles reach the target. Not only the total deposition rate, but also the local deposition pattern in the respiratory tract, is crucial for the clinical success of an inhalation therapy (Sakai et al. 2015; Sznitman et al. 2010). For instance, medications are expected to be delivered to the bronchial or bronchiolar airways in asthmatic patients, while to the alveolar region in emphysema patients (Darquenne et al. 2016). Therefore, it is important to quantify

J. Xi (✉) · T. Yang · K. Talaat · T. Wen · Y. Zhang · S. Klozik · S. Peters
School of Engineering and Technology, Central Michigan University, 1200 South Franklin Street, Mount Pleasant, MI 48858, USA
E-mail: xi1j@cmich.edu
Tel.: (989) 774-2456

the aerosol deposition distribution (ADD) among anatomical regions of the respiratory airway. An accurate knowledge of the ADD can help elucidate the dose–response relationship and facilitate the evaluation of the efficacy of the inhaled pharmaceuticals. As a result, an optimized ADD is expected to maximize the delivered dose to the target and minimize the drug loss in other regions, thereby increasing drug effectiveness and reducing the side effects, drug cost, and treatment time.

Due to the inaccessibility of respiratory tract to conventional measurement instruments, characterizing the ADD within the respiratory tract has generally been conducted using either radioactive imaging in human subjects (Dolovich 2001) or computational modeling in respiratory airway models (Inthavong et al. 2006; Zhang and Martonen 1997). Current imaging techniques to visualize ADD comprise gamma scintigraphy, single photon emission computerized tomography (SPECT), and positron emission tomography (PET). Two types of radioactively labeled aerosols were used to track particle deposition within the body. The 2D gamma scintigraphy and 3D SPECT rely on gamma emitters (technetium-99m), whereas the PET works with positron emitters (fluorine-18) and provides higher 3D spatial details than SPECT (Dolovich and Bailey 2012; Fleming et al. 2015). When used with high-resolution computed tomography (HRCT), SPECT and PET can provide valuable information on 3D ADD in different regions of the lung and is helpful in correlating the ADD with clinical efficacy (De Backer et al. 2010). The downsides of the imaging techniques are their cost, availability, operational complexity, and health risk from radiation (Darquenne et al. 2016; Xi et al. 2016d). Producing adequate radiolabels (technetium-99m) and keeping them attached to aerosols during the entire imaging period is not easy and requires professional operations (Newman et al. 2012). Image blurring due to limited resolution and lung motion is also a problem. More importantly, SPECT and PET can only give the spatial distribution of aerosols, not the distribution relative to the lung anatomy; they need to work with HRCT to obtain the regional doses of aerosols in the lung. Magnetic Resonance imaging (MRI) of ADD has also been reported, but is still in the development phase (Thompson and Finlay 2012). Therefore, it is highly desirable to develop a method to visualize ADD in human airways that is cost-efficient, readily available, easy-to-use, and radiation-free (Inthavong et al. 2016).

Computational fluid dynamics (CFD) modeling has been widely adopted in the past decade to investigate respiratory airflow and aerosol dynamics. Previous CFD studies have explored ADD in different anatomical regions of the human respiratory tract, including the nose, mouth, tracheobronchial region, and deep lungs (Longest and Xi 2007b; Xi and Longest 2008) as well as among different species such as rats, rabbits, and monkeys (Corley et al. 2012; Dong et al. 2016; Xi et al. 2016a, b). Besides ADD visualization, CFD can also yield detailed information on airflow and particle motions, which shed valuable light on the deposition mechanism and provide guidelines in designing inhalation devices. However, CFD often relies on idealized assumptions and neglect many presumably secondary factors to avoid the otherwise prohibitive computational resources incurred. Most previous studies only considered monodisperse particle, steady inhalation, and simplified airway geometry; aerosols were either treated as large inertia particles or small diffusive particle or vapor, with the electric charge, hygroscopy, and size distribution generally neglected. For example, for the dry powder inhaler (DPI) or metered dosed inhaler (MDI), the complex processes of aerosol generation and dynamics immediately after administration make numerical modeling challenging and computationally demanding. Even though it is understandable to model a simplified case, it is reminded that CFD cannot completely mimic the process of most inhalation devices, but can only capture the deposition mechanisms defined by the assumptions adopted in the simulation. When studying the difference of ADD among devices, it is still preferable to conduct experiments using in vitro airway models to predict in vivo dosages for a given combination of device, breathing condition, and formulation (Byron et al. 2010).

Sar-Gel (Sartomer Arkema Group, Exton, PA) has been used to qualitatively visualize the particle deposition patterns due to its color-changing nature upon contact with water(Guo et al. 2005; Kundoor and Dalby 2010, 2011). Studies demonstrated that Sar-Gel had a high sensitivity to droplets from nasal sprays and nebulizers and reacted with water volumes as low as 0.5 μL (Kundoor and Dalby 2010, 2011). Recently, Xi et al. (2016d) visualized the deposition patterns from different types of nebulizers and nasal spray pumps in a hollow nasal airway replica using Sar-Gel. A Sar-Gel image is composed of varying color depths, which represents the distribution of deposited vapor mass. The fact that Sar-Gel is highly sensitive to water suggests that Sar-Gel can be used to visualize ADD of nebulized aerosols in in vitro airway models, and therefore can serve as an alternative to more expensive imaging techniques like gamma scintigraphy, SPECT, or PET to test nebulizer deliveries.

The objective of this study is to develop and validate a technique to visualize nebulized aerosol deposition in human upper respiratory airway geometries. Advantages of both in vitro experiment
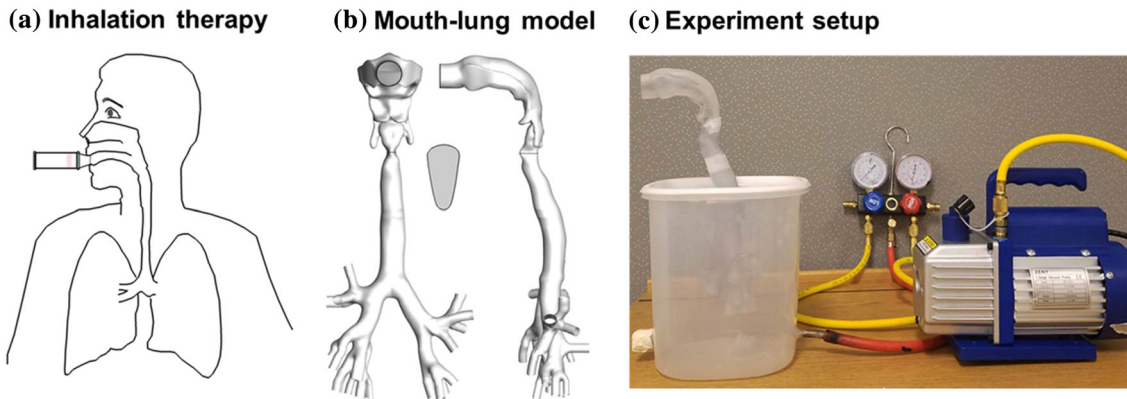
Fig. 1 Experimental test for visualization of upper airway deposition: **a** diagram of inhalation therapy, **b** image-based mouth–lung model that extends to lung bifurcation G6, and **c** experimental set-up to simulate drug delivery under constant inhalation conditions

(inclusive) and computational modeling (detail) will be leveraged to investigate the variation of ADD with different nebulizers and inhalation conditions. Specific aims are: (1) develop an experimental platform for deposition visualization using Sar-Gel in an image-based mouth–lung geometry model; (2) qualitatively validate the in vitro deposition patterns with computational simulations, and (3) compare the differences of deposition pattern of nebulized aerosols with different inhalation rates and different nebulizers.

2 Methods and materials

2.1 Mouth–lung airway model

To visualize the aerosol deposition distribution (ADD) within the upper respiratory airway, an anatomically accurate mouth–lung model that was previously developed will be used in this study. Details of the model dimensions and development procedures can be found in Xi and Longest (2007) and (Xi et al. 2008). Briefly, CT scans of the upper airway were processed in the segmentation software MIMICS (Materialise, Ann Arbor MI) to obtain the polyline contours of the airway. The CT scans of the lung cast were obtained with 0.7 mm slice spacing and 512×512 pixel resolution (Xi et al. 2008). A surface geometry model was then constructed from the contours using Gambit (Ansys, Inc.). Small branches less than 3 mm in diameter were excluded, because of the poor resolution of the CT scans. There are twenty-three branch outlets in the lung model (Fig. 1). The final mouth–lung model was then used to generate a computational mesh for numerical simulations and develop in vitro hollow casts using 3-D printing for experimental purposes.

2.2 Computational simulations

ANSYS ICEM 10 (Ansys, Inc.) was used to generate computational meshes in the mouth–lung model. Smoothing of the geometric surface was performed to avoid excessive mesh size. Considering the geometry complexity, a tetrahedral mesh was created with body-fitted prismatic cells in the near-wall region. The final mesh contained 3.6 million cells, which was sufficient to yield mesh-independent results based on the previous mesh sensitivity studies of the same mouth–lung model (Xi et al. 2013).

Constant inhalations were assumed in this study. The flows were assumed incompressible and isothermal. The Reynolds number at the glottis is 4967, based on an inhalation rate of 30 L/min and a glottal cross-sectional area of 96.5 mm^2. Large eddy simulations (LES) were conducted to resolve the airflow and vortex structures (Si et al. 2013; Xi et al. 2014b). Discrete Lagrangian algorithm was used to track particle trajectories in the flow field at the final computational time (1.5 s). The particle diameter considered in this study was 3.2 μm, which is typical of the vibrating mesh nebulizer output (Dhand 2002; Waldrep and Dhand 2008). The simulations of airflow and particle dynamics were conducted using ANSYS Fluent (Canonsburg, PA). This Lagrangian model, in combination with the near-wall correction treatment, (Longest and Xi 2007a) has been shown in our previous studies to agree with in vitro deposition results in human upper airways for both nanoparticles and micrometer particles (Kim et al. 2014; Li et al. 2007).

2.3 In vitro experiment design

2.3.1 Cast preparation

Software Magics (Materialise, Ann Arbor, MI) was utilized to develop the shell-type hollow casts from the mouth–lung surface model. A constant shell thickness of 4 mm was selected. The mouth–lung replicas were fabricated using a 3-D printer (Stratasys Objet30 Pro, Northville, MI), which has a very high resolution with a printing layer being 16 μm (0.0006 in) in thickness. A transparent material, polypropylene (Veroclear, Northville, MI), was used, so that the particle deposition inside the cast could be visualized from the exterior of the cast. The mouth–lung cast consisted of five major components: the left and right parts of the oral cavity, the larynx, and the left and right parts of the tracheobronchial (TB) region. There was a step-shaped groove at the two interfaces of each section for quick assembly and air-proof sealing. Splitting the oral cavity and lung (TB region) into two parts allows direct visualization of the deposition distribution of nebulized aerosols within these regions.

2.3.2 Experimental set-up and materials

The in vitro lung breathing apparatus is displayed in Fig. 1c. The lung cast was put in a sealed container of 5 L, which was equivalent to the total lung volume of a typical adult male (Jones and Nzekwu 2006). To simulate the steady inhalations during drug delivery, a vacuum pump (Robinair, Warren, MI) was linked to the bottom of the container to simulate constant breathing. The inhalation flow rate was controlled by a flow meter (Omega, Stamford, CT). The nebulized aerosols were introduced into the mouth opening and traveled through the mouth–lung structure (Fig. 1b). To visualize the aerosol deposition distribution, Sar-Gel was spread evenly with a gloved fingertip to the inner surfaces of the cast. For spaces inaccessible to the fingertip such as the small bronchioles, a brush was used to apply the Sar-Gel. After the drug administration, a photo of the mouth–lung cast with Sar-Gel was taken immediately. Control trials were also performed by exposing the Sar-Gel-applied casts to the ambient air. No discernible variation in the Sar-Gel color was observed within 5 min, which is longer than the time needed to complete one test. This observation was corroborated by Kundoor and Dalby (2010, 2011), who observed that Sar-Gel was insensitive to ambient moisture.

2.3.3 Nebulizers

Three nebulizers representative of various types of aerosol-generating techniques were used to conduct each test: Drive Voyager Pro nebulizer (mesh type), Respironics Ultrasonic nebulizer (ultrasonic-type), and Philips InnoSpire Essence nebulizer (jet-type), as illustrated in Fig. 2a. Albuterol sulfate was used as the model drug with a concentration of 0.1% *w/v*. The mesh nebulizer generates monodisperse micrometer droplets ($\sim$ 3.2 μm) by pushing the liquid through a vibrating mesh. In contrast, the ultrasonic nebulizer generates aerosols by implementing ultrasonic vibrations to the solution. The aerosol output from each nebulizer was quantified by activating the nebulizer for certain durations and measuring the nebulizer weight difference before and after the activation. Five trials were repeated for each test to calculate the standard deviations of the aerosol outputs.

3 Results

3.1 Characterization of nebulizer dose outputs

Aerosol outputs were compared among the three nebulizers considered in this study. Soft mists were noted from the ultrasonic and mesh nebulizers, while a fast-moving jet plume was observed from the jet nebulizer (Fig. 2a). A downward motion of aerosols from the ultrasound nebulizer was noticed after administration, possibly due to the large size and low speed of the aerosol particles. The aerosol outputs between nebulizers were compared in Fig. 2b based on five trials for each output. For each nebulizer, a linear profile and small deviations were observed in the aerosol output as a function of time, indicating a consistent performance. However, dose outputs differ significantly among the three nebulizers, with the ultrasonic nebulizer generating the largest amount of aerosols, while the jet nebulizer generating the least amount (Fig. 2b).
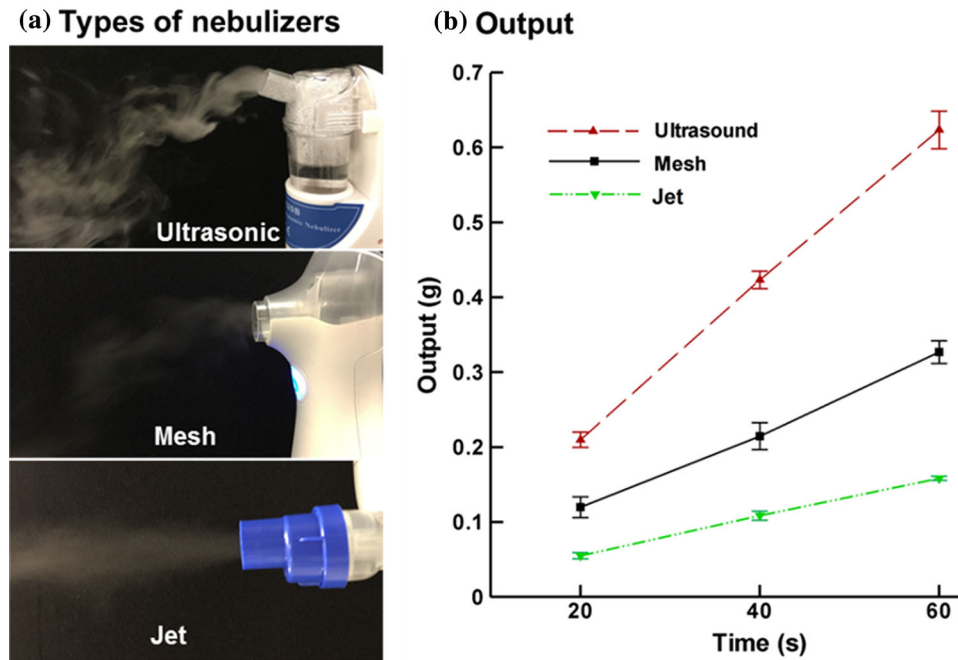
Fig. 2 Nebulizers: **a** three types of nebulizer: ultrasound, mesh, and jet, and **b** nebulized aerosol outputs as a function of time

3.2 Comparison of in vitro and computationally predicted deposition patterns

Comparison of ADDs between in vitro experiments and computational predictions is shown in Fig. 3. The nebulizer used was mesh type and the inhalation flow rate was 30 L/min. Overall, the experimental and computational depositions resemble each other to a high degree, suggesting that the CFD model in this study did capture the mechanisms of particle transport and deposition.

In addition to the similarity in overall patterns, there are nine locations that exhibit highly similar local patterns between the in vitro and computational results, as listed in Fig. 3a, b, and c. For instance, the computational model successfully predicted deposition hot spots in the tip of the glottis (point 1) as well as downstream of the glottis (point 2) (Fig. 3a). In particular, the two stripes in the middle trachea (point 3) match well between the in vitro and CFD results. There was elevated deposition in the first lung bifurcation (carina ridge, point 4); however, the CFD appeared to slightly over-predict the deposition in this region. Similar elevated depositions were also measured and predicted in the lateral larynx (point 5), the roof of the oral cavity (points 6, 7), the dorsal pharynx (point 8), and the back of the carina ridge (point 9) (Fig. 3b, c).

3.3 Deposition visualization of flow rate effect

The deposition pattern inside the mouth–lung cast in Fig. 3 is further illustrated in Fig. 4a in terms of the cut-open view with five parts. Because the cut-open view directly displays the aerosol deposition on the inner airway wall, the deposition pattern has no bias from the cast transparency and thus is more accurate in visualizing the deposition of the delivered drugs. Furthermore, because the depth of the pink color is correlated with the deposition rate in that region, the actual dosage of the delivered medication and the delivery efficiency can be quantified (Xi et al. 2016d). To study the influence of the breathing condition on aerosol deposition, a lower inhalation flow rate (10 L/min) was tested, as shown in Fig. 4b. In comparison to 30 L/min, strikingly different patterns of deposition were attained at 10 L/min. First, a less amount of aerosol was observed to deposit in the oral cavity. This was expected because of the reduced inertia of inhaled aerosols. Second, more aerosols deposited in the trachea and the bronchus due to the increased residence time of aerosol droplets. Moreover, the deposition in the trachea and bronchus were more homogeneous at 10 L/min than at 30 L/min.
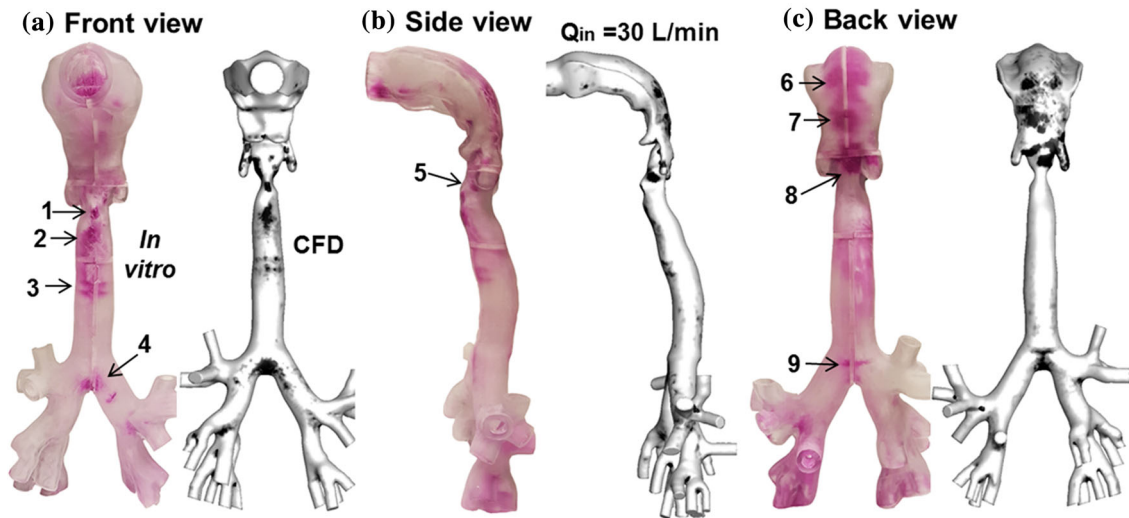
Fig. 3 Comparison of deposition pattern between the in vitro experiments and computational predictions: **a** front view, **b** side view, and **c** back view. The inhalation rate was 30 L/min
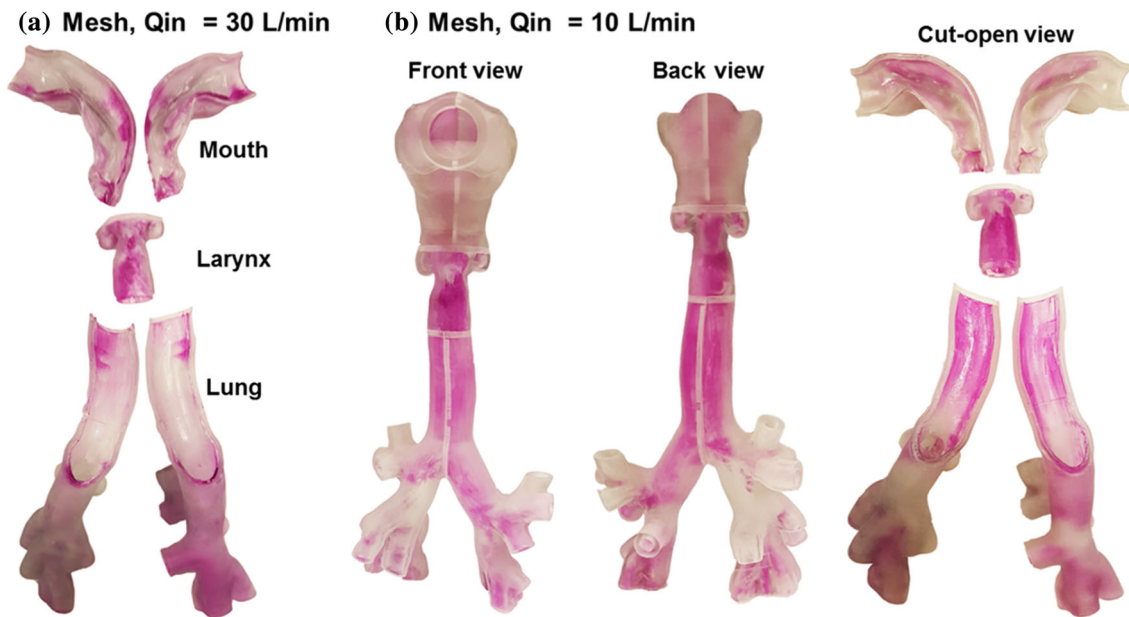

Fig. 4 Comparison of the deposition pattern from a mesh nebulizer at two different inhalation rates: **a** 30 L/min, and **b** 10 L/min

3.4 Deposition visualization for different nebulizers

The developed Sar-Gel visualization method was also extended to study the influence of nebulizer type on drug deliveries. Two additional types of nebulizers, ultrasound and jet, were tested under normal inhalation conditions (30 L/min), as shown in Fig. 5. Comparing Fig. 5 to Figs. 3 and 4, there are both similarities and discrepancies in the deposition patterns using the three types of nebulizers. In comparison to the uniform distribution at lower inhalation rate (10 L/min, Fig. 4b), the deposition patterns are more heterogeneous (or localized) at 30 L/min, regardless of the nebulizer type.

On the other hand, the differences among the three types of nebulizers are also obvious even under the identical inhalation conditions. For both the ultrasound and mesh nebulizers, appreciable deposition in the oral cavity roof was observed, whereas particle deposition in this region was much less significant using the
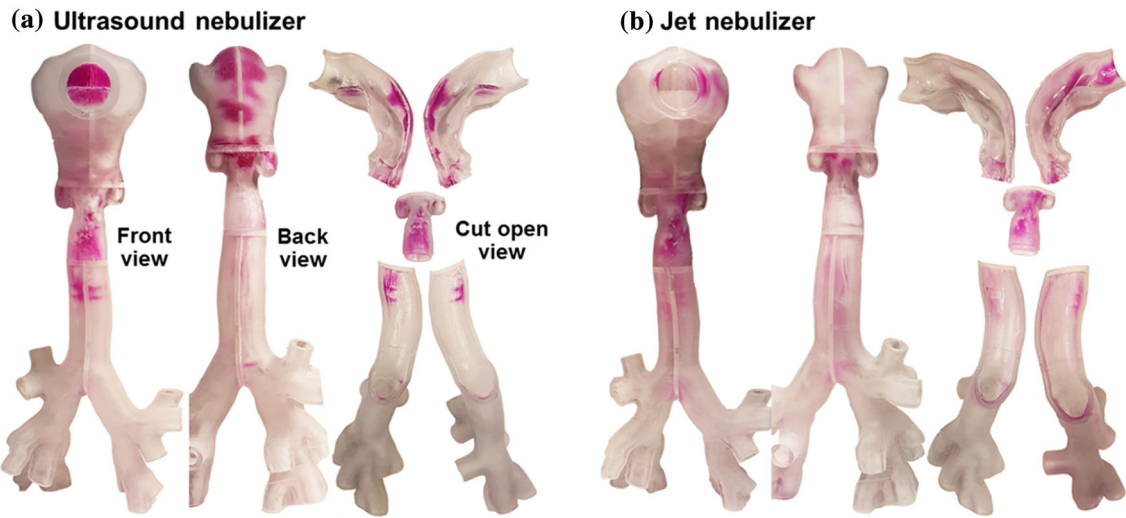
Fig. 5 Comparison of deposition patterns between different types of nebulizers at 30 L/min: **a** ultrasound and **b** jet nebulizer
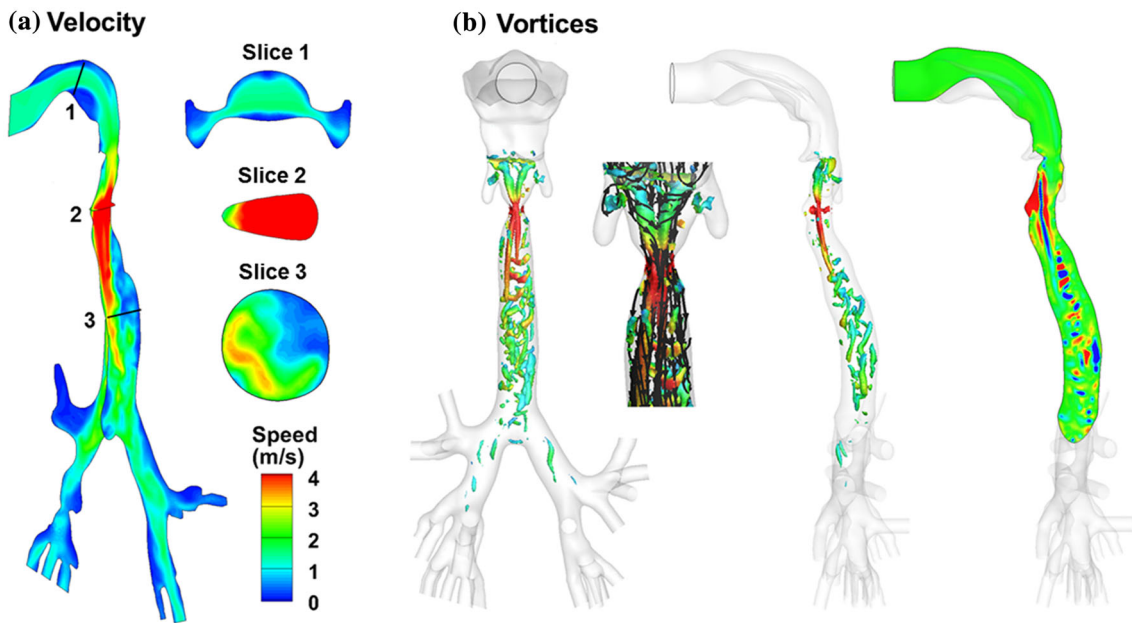

Fig. 6 Computationally predicted **a** velocity field and **b** coherent vortice structures in the mouth–lung airway model at an inhalation flow rate of 30 L/min

jet nebulizer. Instead, elevated levels of deposition in the lateral oral cavity were observed. Particle deposition in the trachea and lungs are also different among the three nebulizers. For instance, there are two stripes of elevated deposition in the upper trachea of both the mesh and ultrasonic nebulizers, while these two stripes are absent in the jet nebulizer.

3.5 Numerical simulations

To gain a better understanding of the experimentally observed deposition patterns, airflows inside the upper airway were simulated and visualized in terms of the velocity field and coherent vortices structures (Fig. 6). Complex flow motions were observed arising from the respiratory anatomical details. First, airflow inhaled through the mouth changed its direction abruptly (90°) in the oral cavity, expecting to cause significant

inertial deposition in the dorsal wall of the velopharynx (Slice 1, Fig. 6a). Recirculation zones were also observed in the oral cavity at the roof of the mouth and downstream of the tongue. Second, a jet flow formed at the glottis due to the sudden airway constriction (Slice 2, Fig. 6a). This high-speed flow (laryngeal jet) persisted into the trachea and led to flow fluctuations. A large recirculation zone within the dorsal trachea was induced by the laryngeal jet, which in turn significantly decreased the area available for the high-speed flow. It was likely that the flow recirculation could prolong the particle resident time and increase particle deposition in that region (Slice 3, Fig. 6a). It was also observed that the flow ventilations into different lobes of the lung were different. The lower lobes received more airflow than the two upper lobes. As administered pharmaceuticals were entrained in the inhaled flow, higher doses were expected in the lower lobes than the upper lobes.

Figure 6b shows the instantaneous coherent structures in the upper airway predicted with large eddy simulation (LES) at 30 L/min. The vortices represent the iso-surfaces of λ_2-criterion at the magnitude of 0.02. Two streamwise vortex filaments are observed to arise from swirling flows upstream of the glottis. These vortices, which act as energy capacitors, require energy and time to initiate, develop, and decay. The two vortex filaments continue to grow after the glottis due to the energy inputs from the laryngeal jet, which induce an array of vortex rings in the upper trachea. This process has an important effect on turbulence generation and pressure drop across the glottis. In the middle trachea, these vortex rings start to decay as the energy input from the laryngeal jet diminishes. Further downstream, the vortex rings break into smaller scale eddies, suggesting that turbulence decreases and relaminarization advances. In the first lung bifurcation, survived eddies preferentially enter the two lower lobes due to their inertia. It is noted that these vortices are oscillating all the time. The alternating high and low energy intensities at one instant are evident in the right panel of Fig. 6b.

The transport of drug particles within the respiratory tract was also examined. Figure 7a shows the pathlines of massless particles within the respiratory airway. The stream traces were colored by the velocity magnitude. By inspecting individual pathlines (Fig. 7a), it is noted that particles released from different locations will generally go to different zones of the lung. Moreover, the particle speed varies along its journey through the respiratory tract, which accelerates before reaching the glottis and decelerates after passing the glottis. Flow instabilities and turbulence are important in the mouth–throat–trachea, but will gradually diminish in the lung bifurcations. When the airflow reaches the lung bifurcation G5-6, the instability or turbulence effect is already insignificant. 3D particle dynamics within the mouth–lung model is visualized in Fig. 7b as snapshots of particle locations at various instants after administration for 3.2 μm aerosols. A majority of particles are observed in regions of high-speed flow, while low particle concentrations occur either within low-speed flow regions or recirculation zones. A thin layer of slow-moving
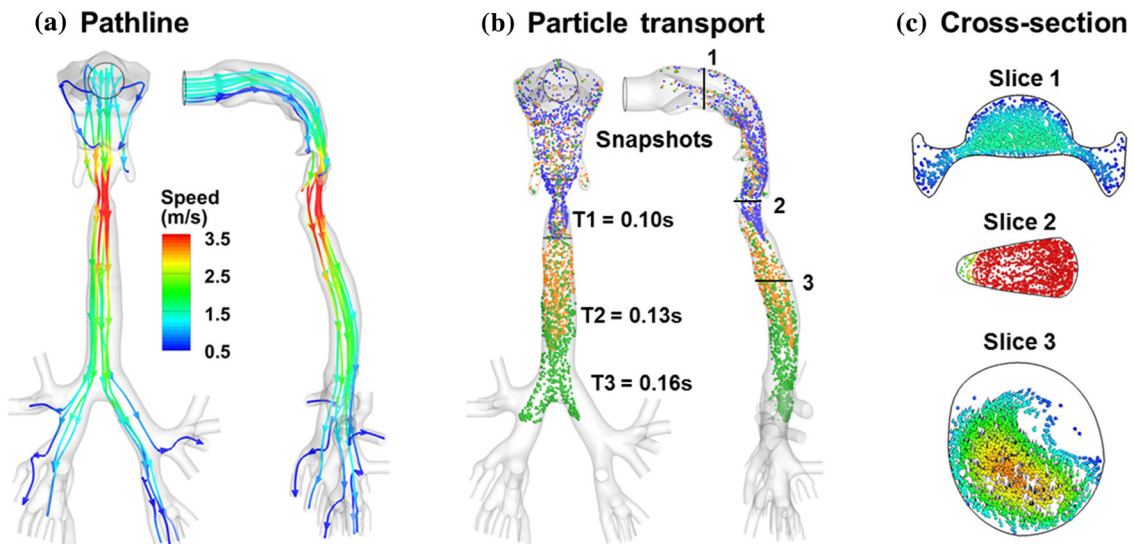

Fig. 7 Particle dynamics: **a** streamlines of massless particles, **b** snapshots of particle locations at various instants after their administration into the mouth, and **c** cross-sectional views of the particle distribution at different locations. The color code in panel (**b**): blue for T1, brown for T2, and green for T3

aerosols is discerned to remain near the geometry walls. Particles start to interact with the first bifurcation at $T = 0.16$ s.

Figure 7c shows the cross-sectional profiles of particles at selected slices along the airway. High concentrations of particles are noted in the core flow region in the mouth, while fewer particles are noted in the near-wall regions (Slice 1, Fig. 7c). In Slice 3, particles are concentrated near the ventral wall of the trachea due to the particle transportation by the high-speed laryngeal jet (Fig. 7c). Accordingly, higher depositions of inhaled particles are expected in the ventral wall of the trachea, which is consistent with the observations of in vitro experiments (Figs. 3, 4, 5).

4 Discussions and conclusion

In this study, a method to directly visualize the aerosol deposition distribution (ADD) in human upper airways was developed. The Sar-Gel approach, along with sectional airway casts, was shown to provide a feasible means to visualize ADD of nebulized droplets inside the respiratory tract. Advances in manufacturing and imaging techniques permit more control over the preparation of airway cast replicas. In this study, an image-based mouth–lung model that had been previously developed from CT scans (Longest and Xi 2008; Xi and Longest 2007) was used to create the hollow cast replicas via 3D printing. To disclose the inner ADD, the mouth–lung airway was separated into five sections (Figs. 4, 5). This sectional cut-open airway replica provided a special advantage to visualize the ADD inside the respiratory tract using fluorescent particles or color-changing gels, which was inaccessible to most measuring instruments. Previous visualization studies have commonly used gamma scintigraphy to characterize the ADD inside human airways. However, because gamma scintigraphy gives 2D images of varying brightness as a function of the particle concentration, it cannot discriminate particle depositions upon overlapping surfaces in the camera direction. Moreover, gamma emitters are needed. Although claimed harmless, gamma emitters still require professional handling and are not readily available, which make this technique not practical for most labs. By contrast, the Sar-Gel based approach is simple, less expensive, and does not need radiolabels. Furthermore, it can directly disclose the ADD and therefore removes the issues, if there are multiple overlapping surfaces.

The results of this study revealed highly heterogeneous aerosol deposition patterns for all nebulizers considered, which changed with different nebulizer types and breathing conditions. The local or regional deposition of therapeutic agents is a more relevant factor in developing a dose–response relationship than the overall deposition rate. Therefore, knowing the ADD is crucial in assessing the medication efficacy, developing new inhalation devices or drug formulations, and optimizing delivery protocols to maximize the doses to the targeted region, while minimizing drug loss to other regions. For instance, using a mesh nebulizer, fewer drug particles deposited in the mouth, while more particles deposited in the trachea and bronchus at 10 L/min than at 30 L/min, as shown in Fig. 4. Thus, if the target is at the central airway (trachea to G6) such as in asthmatic patients, inhaling at 10 L/min will reduce the drug losses in the oral cavity and increase the delivered doses to the central airway relative to inhaling at 30 L/min.

The ADD has been qualitatively demonstrated to agree well between the Sar-Gel visualization and corresponding computational predictions. In additiona to the similarity in overall deposition patterns between the experiments and computation, the local deposition hot spots also match each other in multiple sites, such as the pharynx, larynx, trachea, and lung bifurcation. In particular, the two stripes of elevated deposition hot spots in the upper trachea match between experiment and modeling to a high degree (Fig. 3a). It is noted that the in vitro hollow cast and computational model in this study were developed from the same mouth–lung airway geometry. The aerosol size (3.2 μm), inhalation rate (30 L/min), and outlet boundary condition (same vacuum pressure) were also identical between the experiment and modeling. Therefore, the agreement of ADD between the Sar-Gel visualization and computational modeling cross-validated each other, that both approaches are capable of capturing the particle transport mechanisms. It is also noted that the proposed Sar-Gel visualization technique can be easily adapted to study pulmonary drug delivery to different respiratory regions (such as the nose, central lung, or deep lung), or under different breathing maneuvers (such as shallow, deep, slow, and fast inhalations).

The proposed Sar-Gel visualization technique and computational fluid dynamics (CFD) modeling can be used complementarily in refining inhalation therapy protocols. Both CFD and Sar-Gel visualization can provide detailed information on deposition distribution. However, both approaches have their inherent advantages and disadvantages. For instance, Sar-Gel visualization characterizes the ADD only in a

Table 1 Comparison of flow distributions between experiments and numerical predictions at 30 L/min

	Left lung			Right lung			
	Lower	Upper	Total	Lower	Middle	Upper	Total
Measured[a] (%)	23.9	15.9	39.8	32.4	9.6	18.2	60.2
CFD[b] (%)	24.3	16.3	40.6	33.2	9.0	17.2	59.4
Deviation (%)	1.7	2.5	2.0	2.5	− 6.3	− 5.6	− 1.3

[a]Measured flow distribution by Cohen et al. (1990) in a cadaver-based lung cast
[b]Numerically predicted flow distribution in a lung model reconstructed from CT scans of the lung cast

qualitative manner, while CFD can characterize the ADD in a quantitative manner and provide detailed information about in flow and particle behaviors that are difficult to observe experimentally. In addition, CFD is more cost-efficient and can simulate scenarios that are either infeasible or too expensive using in vitro tests. On the other hand, Sar-Gel visualization can mimic pulmonary drug deliveries in a more clinically relevant manner. With an anatomically accurate mouth–lung model, the clinical factors associated with nebulizers and breathing conditions can be readily duplicated in the Sar-Gel visualization tests. These include the aerosol size distribution, electric charges of the nebulized droplets, evaporation or hygroscopy of inhaled droplets within the respiratory airway, tidal breathing conditions, airway compliance, and inter-test variability in nebulizer outputs. Even though these clinical factors are possible to be considered in CFD, either tremendous computational resources or advanced computational models are needed. Recent CFD studies have attempted to incorporate the influences of polydisperse aerosols (Xi et al. 2016c), electric charges (Xi et al. 2014a), hygroscopy (Kim et al. 2013; Zhang et al. 2006), and tidal breathing (Zhang and Kleinstreuer 2002). However, numerical attempts that simulate particle deposition under the influences of a dynamic airway (oral cavity or glottis) or a certain level of uncertainty in nebulizer outputs have not yet been reported.

One limitation in this study was the application of equal pressure at all outlets in the experiments. Several in vitro studies were conducted to quantify the outflow distribution in lung casts. Cohen and Briant (1989) compared to flow distribution in airway casts for constant and cyclic flows and showed no significant distribution differences between the two flow patterns. Detailed flow distributions among all outlets were also measured in a cadaver-based lung cast by Cohen et al. (1990). Noting that the computational lung model in this study was a direct reproduction of the in vitro cast used by Cohen et al. (1990). It was also shown that flow partitions among the lobes did not change significantly as flow rates increased, justifying a constant outflow partition for varying flow rates (Cohen et al. 1993). The application of equal outlet pressures herein was due to the technical challenges to match the outflow distributions as measured by Cohen et al. (1990), which required 23 vacuums in this study. To quantify the influence from this limitation, predicted flow partition among the 23 outlets under equal outlet pressure condition was compared to the experimental measurements by Cohen et al. (1990) in a comparable lung cast. Results show that the flow ventilation into the left and right lobes herein matches well with Cohen's measurements, with the left and right lungs receiving 40.6 and 59.4% (versus 39.8 and 60.2% in measurements), respectively. This ventilation ratio is also consistent with the in vivo measurements by Frerichs et al. (2006). The flow ventilation among the five lobes in this lung model also agrees with the measurements of Cohen et al. (1990) to an acceptable level, which ranges from − 6.3 to 2.5%, as shown in Table 1. It is noted that the left–right ventilation ratio can vary with age and health of the subject. A fraction of 69% of total inhalation was observed into the right lung and 31% into the left lung after airway injury (Frerichs et al. 2006). In contrast, Alderson et al. (1976) measured ventilation distribution in 12 children from 9-month to 4-year old and reported 53 ± 2% to the right lung and 47 ± 2% to the left. Recently, deriving lung ventilation distribution from 4-dimensional CT becomes feasible (Latifi et al. 2013). However, reports of explicit ventilation distribution among left–right lungs, lobes, or bronchioles have not been found yet. An alternative method to include the lower airway effects is to use a tubular resistor and a balloon following each outlet with comparable resistance and compliance, as demonstrated by Han and Hirahara (2016).

In the computational model, an equal pressure condition was implemented for the 23 outlets to gain a better understanding of the experimentally observed deposition patterns. However, specifying a physiologically realistic outflow condition for lung bifurcations is more complex than this. Depending on the shape and size of the bronchioles, the outlet pressures will be heterogeneous to varying degrees. Similarly, the outflow distributions can be neither uniform in space nor constant in time. It is generally accepted that lower lobes are better ventilated than upper lobes due to lower flow resistances. In previous numerical studies,

outflows had been assumed to have either uniform pressures, uniform velocities, being proportional to the fraction of the total lung volume subtended by each airway, or including the resistance and compliance of the subtended airways (Han et al. 2016; Hirahara et al. 2011; Ma and Lutchen 2006). Even though adopting equal outlet pressures matched the experimental condition in this study, the resistance and compliance of lower airways should be considered in future studies to better approximate the in vivo scenarios.

Several other assumptions may also affect the applicability of the results in this study. These assumptions include steady flows, rigid airway cast, a lung model extending to G5-6, and a model representative of a healthy lung only. Previous studies have highlighted the influences on ADD from transient inhalation (Xi et al. 2008) and compliant airway surfaces (Berg et al. 2010). The lung model was reconstructed from a cadaver-based lung cast and might be different from a living lung. Significant difference in airflows can exist between healthy and diseased airways, as demonstrated by Kim et al. (2009), who visualized gas transfer in a bronchiole model with stenosis. Considering the ubiquitous uncertainty and complexity in variables related to drug particles, device, and patient, fully simulating the delivery process is still impractical (Courrier et al. 2002; Labiris and Dolovich 2003a, b). These sources of uncertainty may be difficult to control and can impact the drug delivery efficiency to varying degrees. Probabilistic analysis can quantify the sensitivity levels of input parameters, as well as the output uncertainties, and should be considered in future studies.

Compliance with ethical standards

Conflict of interest The authors report no conflicts of interest in this work.

References

Alderson PO, Boonvisut S, McKnight RC, Hartman AF (1976) Pulmonary perfusion abnormalities and ventilation-perfusion imbalance in children after total repair of tetralogy of Fallot. Circulation 53:332–337

Berg EJ, Weisman JL, Oldham MJ, Robinson RJ (2010) Flow field analysis in a compliant acinus replica model using particle image velocimetry (PIV). J Biomech 43:1039–1047

Byron PR, Hindle M, Lange CF, Longest PW, McRobbie D, Oldham MJ, Olsson B, Thiel CG, Wachtel H, Finlay WH (2010) In vivo-in vitro correlations: predicting pulmonary drug deposition from pharmaceutical aerosols. J Aerosol Med Pulm Drug Deliv 23:59–69

Cohen B, Briant J (1989) Flow distribution in human and canine tracheobronchial airway casts. Health Phys 57:21–27

Cohen BS, Sussman RG, Lippmann M (1990) Ultrafine particle deposition in a human tracheobronchial cast. Aerosol Sci Technol 12:1082–1093

Cohen BS, Sussman RG, Lippmann M (1993) Factors affecting distribution of airflow in a human tracheobronchial cast. Respir Physiol 93:261–278

Corley RA, Kabilan S, Kuprat AP, Carson JP, Minard KR, Jacob RE, Timchalk C, Glenny R, Pipavath S, Cox T, Wallis CD, Larson RF, Fanucchi MV, Postlethwait EM, Einstein DR (2012) Comparative computational modeling of airflows and vapor dosimetry in the respiratory tracts of rat, monkey, and human. Toxicol Sci 128:500–516

Courrier HM, Butz N, Vandamme TF (2002) Pulmonary drug delivery systems: recent developments and prospects. Crit Rev Ther Drug Carr Syst 19:425–498

Darquenne C, Fleming JS, Katz I, Martin AR, Schroeter J, Usmani OS, Venegas J, Schmid O (2016) Bridging the gap between science and clinical efficacy: physiology, imaging, and modeling of aerosols in the lung. J Aerosol Med Pulm Drug Deliv 29:107–126

De Backer JW, Vos WG, Vinchurkar SC, Claes R, Drollmann A, Wulfrank D, Parizel PM, Germonpre P, De Backer W (2010) Validation of computational fluid dynamics in CT-based airway models with SPECT/CT. Radiology 257:854–862

Dhand R (2002) Nebulizers that use a vibrating mesh or plate with multiple apertures to generate aerosol. Respir Care 47:1406–1416

Dolovich MB (2001) Measuring total and regional lung deposition using inhaled radiotracers. J Aerosol Med 14:S35–S44

Dolovich MB, Bailey DL (2012) Positron emission tomography (PET) for assessing aerosol deposition of orally inhaled drug products. J Aerosol Med Pulm Drug Deliv 25:S52–S71

Dong J, Shang Y, Inthavong K, Tu J, Chen R, Bai R, Wang D, Chen C (2016) Comparative Numerical modeling of inhaled nanoparticle deposition in human and rat nasal cavities. Toxicol Sci 152:284–296

Fleming J, Conway J, Majoral C, Katz I, Caillibotte G, Pichelin M, Montesantos S, Bennett M (2015) Controlled, parametric, individualized, 2-D and 3-D imaging measurements of aerosol deposition in the respiratory tract of asthmatic human subjects for model validation. J Aerosol Med Pulm Drug Deliv 28:432–451

Frerichs I, Dargaville PA, van Genderingen H, Morel DR, Rimensberger PC (2006) Lung volume recruitment after surfactant administration modifies spatial distribution of ventilation. Am J Respir Crit Care Med 174:772–779

Guo Y, Laube B, Dalby R (2005) The effect of formulation variables and breathing patterns on the site of nasal deposition in an anatomically correct model. Pharm Res 22:1871–1878

Han B, Hirahara H (2016) Effect of gas oscillation-induced irreversible flow in transitional bronchioles of human lung. J Flow Control Meas Vis 4:171–193

Han B, Hirahara H, Yoshizaki S (2016) Streaming caused by oscillatory flow in peripheral airways of human lung. Open J Fluid Dyn 6:242–261

Hirahara H, Iwazaki K, Ahmmed MU, Nakamura M (2011) Numerical analysis of air flow in dichotomous respiratory channel with asymmetric compliance under HFOV condition. J Fluid Sci Technol 6:932–948

Inthavong K, Tian ZF, Li HF, Tu JY, Yang W, Xue CL, Li CG (2006) A numerical study of spray particle deposition in a human nasal cavity. Aerosol Sci Technol 40:1034

Inthavong K, Tao Y, Petersen P, Mohanarangam K, Yang W, Tu J (2016) A smoke visualisation technique for wake flow from a moving human manikin. J Vis 19:1–13

Jones RL, Nzekwu MMU (2006) The effects of body mass index on lung volumes. Chest 130:827–833

Kim J-K, Kawahashi M, Hirahara H, Iwasaki Y (2009) Experimental analysis of oscillatory airflow in a bronchiole model with stenosis. J Vis 12:109–118

Kim J, Xi J, Si XA (2013) Dynamic growth and deposition of hygroscopic aerosols in the nasal airway of a 5-year-old child. Int J Numer Meth Biomed Eng 29:17–39

Kim J, Xi J, Si X, Berlinski A, Su WC (2014) Hood nebulization: effects of head direction and breathing mode on particle inhalability and deposition in a 7-month-old infant model. J Aerosol Med Pulm Drug Deliv 27:209–218

Kundoor V, Dalby RN (2010) Assessment of nasal spray deposition pattern in a silicone human nose model using a color-based method. Pharm Res 27:30–36

Kundoor V, Dalby RN (2011) Effect of formulation- and administration-related variables on deposition pattern of nasal spray pumps evaluated using a nasal cast. Pharm Res 28:1895–1904

Labiris NR, Dolovich MB (2003a) Pulmonary drug delivery. Part I: physiological factors affecting therapeutic effectiveness of aerosolized medications. Br J Clin Pharmacol 56:588–599

Labiris NR, Dolovich MB (2003b) Pulmonary drug delivery. Part II: the role of inhalant delivery devices and drug formulations in therapeutic effectiveness of aerosolized medications. Br J Clin Pharmacol 56:600–612

Latifi K, Feygelman V, Moros EG, Dilling TJ, Stevens CW, Zhang GG (2013) Normalization of ventilation data from 4D-CT to facilitate comparison between datasets acquired at different times. PLoS ONE 8:e84083

Li Z, Kleinstreuer C, Zhang Z (2007) Simulation of airflow fields and microparticle deposition in realistic human lung airway models. Part II: particle transport and deposition. Eur J Mech B 26:650–668

Longest PW, Xi J (2007a) Computational investigation of particle inertia effects on submicron aerosol deposition in the respiratory tract. J Aerosol Sci 38:111–130

Longest PW, Xi J (2007b) Effectiveness of direct Lagrangian tracking models for simulating nanoparticle deposition in the upper airways. Aerosol Sci Technol 41:380–397

Longest PW, Xi JX (2008) Condensational growth may contribute to the enhanced deposition of cigarette smoke particles in the upper respiratory tract. Aerosol Sci Technol 42:579–602

Ma B, Lutchen KR (2006) An anatomically based hybrid computational model of the human lung and its application to low frequency oscillatory mechanics. Ann Biomed Eng 34:1691–1704

Newman S, Bennett WD, Biddiscombe M, Devadason SG, Dolovich MB, Fleming J, Haeussermann S, Kietzig C, Kuehl PJ, Laube BL, Sommerer K, Taylor G, Usmani OS, Zeman KL (2012) Standardization of techniques for using planar (2D) imaging for aerosol deposition assessment of orally inhaled products. J Aerosol Med Pulm Drug Deliv 25(Suppl 1):S10–S28

Sakai H, Watanabe Y, Sera T, Yokota H, Tanaka G (2015) Visualization of particle deposition in human nasal cavities. J Vis 18:349–357

Si X, Xi J, Kim J (2013) Effect of laryngopharyngeal anatomy on expiratory airflow and submicrometer particle deposition in human extrathoracic airways. Open J Fluid D 3:286–301

Sznitman J, Sutter R, Altorfer D, Stampanoni M, Rosgen T, Schittny JC (2010) Visualization of respiratory flows from 3D reconstructed alveolar airspaces using X-ray tomographic microscopy. J Vis 13:337–345

Thompson RB, Finlay WH (2012) Using MRI to measure aerosol deposition. J Aerosol Med Pulm Drug Deliv 25:55–62

Waldrep JC, Dhand R (2008) Advanced nebulizer designs employing vibrating mesh/aperture plate technologies for aerosol generation. Curr Drug Deliv 5:114–119

Xi J, Longest PW (2007) Transport and deposition of micro-aerosols in realistic and simplified models of the oral airway. Ann Biomed Eng 35:560–581

Xi J, Longest PW (2008) Numerical predictions of submicrometer aerosol deposition in the nasal cavity using a novel drift flux approach. Int J Heat Mass Transfer 51:5562–5577

Xi J, Longest PW, Martonen TB (2008) Effects of the laryngeal jet on nano- and microparticle transport and deposition in an approximate model of the upper tracheobronchial airways. J Appl Physiol 104:1761–1777

Xi J, Kim J, Si XA, Zhou Y (2013) Diagnosing obstructive respiratory diseases using exhaled aerosol fingerprints: a feasibility study. J Aerosol Sci 64:24–36

Xi J, Si X, Gaide R (2014a) Electrophoretic particle guidance significantly enhances olfactory drug delivery: a feasibility study. PLoS ONE 9:e86593

Xi J, Si X, Kim J, Su G, Dong H (2014b) Modeling the pharyngeal anatomical effects on breathing resistance and aerodynamically generated sound. Med Biol Eng Comput 52:567–577

Xi J, Kim J, Si XA, Corley RA, Zhou Y (2016a) Modeling of inertial depositions in scaled models of rat and human nasal airways: towards in vitro regional dosimetry in small animals. J Aerosol Sci 99:78–93

Xi J, Si XA, Kim J, Zhang Y, Jacob RE, Kabilan S, Corley RA (2016b) Anatomical details of the rabbit nasal passages and their implications in breathing, air conditioning, and olfaction. Anat Rec 299:853–868

Xi J, Yuan JE, Si XA (2016c) Simulation study of electric-guided delivery of 0.4 μm monodisperse and polydisperse aerosols to the ostiomeatal complex. Comput Biol Med 72:1–12

Xi J, Yuan JE, Zhang Y, Nevorski D, Wang Z, Zhou Y (2016d) Visualization and quantification of nasal and olfactory deposition in a sectional adult nasal airway cast. Pharm Res 33:1527–1541

Zhang Z, Kleinstreuer C (2002) Transient airflow structures and particle transport in a sequentially branching lung airway model. Phys Fluids 14:862–880

Zhang Z, Martonen TB (1997) Deposition of ultrafine aerosols in human tracheobronchial airways. Inhal Toxicol 9:99–110

Zhang Z, Kleinstreuer C, Kim CS (2006) Water vapor transport and its effects on the deposition of hygroscopic droplets in a human upper airway model. Aerosol Sci Technol 40:52–67